NJC

PAPER

View Article Online
View Journal | View Issue

Cite this: *New J. Chem.*, 2022, **46**, 17967

Zinc stannate microcubes with an integrated microheater for low-temperature NO_2 detection†

Nirav Joshi, *[ab] Hu Long,[cd] Pranav Naik,[e] Arvind Kumar,[f] Valmor R. Mastelaro,[b] Osvaldo N. Oliveira Jr,[b] Alex Zettl[d] and Liwei Lin[a]

Received 1st June 2022,
Accepted 23rd August 2022

DOI: 10.1039/d2nj02709g

rsc.li/njc

This paper reports a facile technique to construct an oxide nanostructured film on a low-power microheater sensor platform to detect NO_2 gas with high sensitivity and selectivity at a low temperature. Microcube-shaped zinc stannate ($ZnSnO_3$) nanostructures prepared through a co-precipitation method were used to detect NO_2 down to 85 ppb at 110 °C with a fast response and recovery time. Specifically, a 192% response in the resistance change was measured for 5 ppm NO_2 gas, with a response time of 3.36 mins, excellent reproducibility, long-term stability, and high selectivity. The good gas-sensing performance of the $ZnSnO_3$ microcubes is due to their porous surface, which provides a large surface area and suitable absorption–desorption processes. The versatility of the $ZnSnO_3$ nanostructures may be further exploited with various sensing units on a single chip towards the development of arrays, as in electronic noses.

1. Introduction

Chemiresistive gas sensors made using metal oxide semiconductors (MOS) on ceramic substrates have been used widely to detect hazardous gases in industrial factories, and in commercial spaces for the monitoring of air quality.[1] However, state-of-art sensors used in these fields are bulky and costly and have high power consumptions (~500 mW), which makes them unsuitable for portable and battery-powered devices since a heater is needed to boost the sensitivity and response/recovery rates.[2,3] To overcome these limitations, miniaturization with microfabrication techniques has been employed to produce small and low-cost devices that have low power requirements.[3] Nanostructured metal oxides with large surface areas and porous structures, including microspheres, microcubes, and nanocages with facile adsorption-desorption processes, have been proposed to increase the sensitivity.[4–8] The choice of nanostructured metal oxides is usually determined by the target gases. For instance, various metal oxides/binary oxides have been investigated, including ZnO, SnO_2, Fe_2O_3, and Co_3O_4.[9–12] The primary challenges with gas sensor devices are their selectivity and operation temperature. Researchers are particularly interested in room-temperature operation, and there have been numerous attempts to increase the selectivity of these sensors. The selectivity towards a specific analyte can be enhanced by adjusting the surface-to-volume ratio, the grain orientation, and the film morphology.[13–15] Other reported methods include substitutional doping, the formation of composites and hybrids with other nanomaterials, such as metal oxides, 2D materials, carbon nanotubes, and so on, as well as chemical functionalization with noble metal nanoparticles. For example, Ma *et al.*[16] reported 3D SiO_2@MWCNT core–shell nanospheres for the highly sensitive detection of nitrogen dioxide gas (NO_2) at room temperature, with a maximum sensitivity of 82.61%. The response time was observed to be 25 min, and they used UV illumination to achieve complete recovery (44 s). Similarly, Zhang *et al.*[17] synthesized In_2O_3 NWs using electrospinning and they reported a high sensing response of 740 at 5 ppm NO_2 in the dark at room temperature. However, they utilized visible-light irradiation to shorten the recovery time (20 s). Huang *et al.*[18] developed a robust NO_2 sensor using SnS_2/rGO nanohybrids, which showed a sensitivity of 650% with a response time of 75 s at room temperature and achieved complete recovery in the visible-light region. UV-light has been utilized to increase the performance of oxide and 2D material-based gas sensors. However, degradation of the structure of the material by UV-light can significantly impair its reproducibility.[19]

Nitrogen dioxide (NO_2) is an air pollutant with a pungent odor and high toxicity, and is generated from fossil fuels in

[a] *Department of Mechanical Engineering, University of California, Berkeley, CA, USA. E-mail: nirav.joshi1986@gmail.com*
[b] *São Carlos Institute of Physics, University of São Paulo, CP 369, São Carlos 13560-970, São Paulo, Brazil*
[c] *Department of Mechatronics Engineering, School of Mechanical Science and Engineering, Huazhong University of Science and Technology, Wuhan, HuBei 430074, China*
[d] *Department of Physics, University of California at Berkeley, Materials Sciences Division, Lawrence Berkeley National Laboratory, Kavli Energy NanoSciences Institute, Berkeley, CA 94720, USA*
[e] *Department of Physics, Goa University, Taleigao Plateau, Goa, 403206, India*
[f] *Department of Physics, Chaman Lal Mahavidyalaya, Haridwar, India*
† Electronic supplementary information (ESI) available. See DOI: https://doi.org/10.1039/d2nj02709g

combustion processes and in chemical plants.[15] Overexposure to this gas can cause respiratory problems, which are particularly harmful to people with asthma.[20–22] The National Institute for Occupational Safety and Health (NIOSH) has set 1 ppm and a short-term limit of 15 min as the emission standard.[23] The demand for sensitive and selective gas sensors that detect NO_2 with a low power consumption has sparked sensor research with the aforementioned metal oxides, but most of these materials have limitations in terms of their operating temperature and selectivity.[9,24,25] Binary metal oxides are those that contain at least one transition metal ion and one or more electrochemically active/inactive ions. However, compared with single-component oxides, binary metal oxides may have a higher redox chemical ability and may integrate contributions from two types of ions to improve the sensing performance.[26–28] Zhou and co-workers[29] synthesized $ZnSnO_3$ hollow cubes with a high sensitivity and selectivity for the detection of ethanol vapor at the ppm level and at an operating temperature of 260 °C. Patil *et al.*[30] reported sensors made with zinc stannate films with a sensor response of 29.3 for a 40 ppm NO_2 concentration and with a fast response and recovery speed at an operating temperature of 200 °C. In the latter case, the room-temperature operation would be possible with the activation of chemical reactions under UV-light irradiation. Dabbabi and co-workers used $ZnSnO_3$ thin films to detect NO_2 at room temperature with a fast response time, although they found unstable baseline resistance changes under UV light irradiation.[31] $ZnSnO_3$ has also been used for detecting volatile organic compounds (VOCs) and toxic analytes at low ppb levels, although its operation temperature is a major concern.[32–35]

In this work, a simple fabrication procedure is presented for the synthesis of $ZnSnO_3$ microcubes together with a low-power microheater to yield an excellent sensing performance for NO_2 gas. The $ZnSnO_3$ microcubes were synthesized using a co-precipitation method and a subsequent annealing process. They were deposited on a microheater platform to enhance the sensor response and selectivity for NO_2 at a low operating temperature. The improved sensing performance is attributed to the large specific surface area of the microtubes, which enables the fast diffusion of gas to the active sites.

2. Experimental section

2.1 Synthesis and materials characterization

$ZnSnO_3$ microcubes were synthesized using a room-temperature co-precipitation method.[29] In a typical synthesis procedure, 0.1 M zinc chloride ($ZnCl_2$) and sodium citrate ($C_6H_5Na_3O_7$) were dissolved in 10 mL deionized (DI) water and the solution was added to 5 mL of a 0.2 M tin chloride ($SnCl_4$) ethanol solution under stirring to form a homogeneous solution. Then, 0.41 M NaOH solution (25 mL) was added dropwise into the homogeneous solution and stirred for 1 h. White precipitates of $ZnSn(OH)_6$ were formed, washed, and centrifuged with water and ethanol 4 times, and left to dry overnight at 80 °C. The powder was placed in a quartz tube and annealed at 450 °C for 2 h in air with heating and cooling rates of 1 °C min^{-1} to obtain the $ZnSnO_3$ cubes. The synthesis procedure is schematically displayed in Fig. S1 in the ESI.† All reagents were of analytical grade and were used without further purification. The morphology of the samples was characterized using field-emission scanning electron microscopy (FE-SEM; Zeiss Sigma) operating at 5 kV, and equipped with X-ray energy dispersive spectroscopy (EDS) for elemental analysis. The crystal structure was characterized using X-ray diffraction (Rigaku, Rotaflex RU-200B) with a Cu Kα target (λ = 0.15406 nm). The chemical composition and the chemical state of the samples were determined *via* X-ray photoelectron spectroscopy (XPS) using an ESCALAB-MKII spectrometer (UK) with Al Kα radiation (1486.6 eV) as the X-ray source for excitation. The pore-size distribution and the specific surface area of the samples were estimated using the Brunauer–Emmett–Teller (BET) method based on the nitrogen adsorption–desorption isotherms (BELSORP-mini II, Japan).

2.2 Sensor device fabrication and gas-sensing measurements

The gas sensors were fabricated by ultrasonically dispersing the as-prepared $ZnSnO_3$ microcubes (10 mg) in 1 mL isopropyl alcohol. The suspension was then drop-cast onto the microsensor substrate containing a circularly shaped sensing area of interdigitated sensing electrodes (with a line width and spacing of 20 μm) encircled by a double meandered Pt heater (line width of 50 μm) to regulate the operating temperature and ensure its uniformity as shown in Fig. 1a and b. For the fabrication process (Fig. 1c),[36] a 4-inch-long Si/SiO_2 wafer was used, and the Pt structure was patterned using standard UV photolithography and lift-off processes. A 10 nm-thick layer of chromium and a 90 nm-thick layer of Pt were deposited *via* physical vapor deposition onto the wafer. The metal lift-off was performed by placing the wafer in *N*-methylpyrrolidone at 60–80 °C for 10 min and rinsing it with 2-propanol before drying. Each 4-inch silicon wafer contains 60–70 microsensor electrodes. The electrodes on the silicon wafer were diced and fixed onto ceramic packages using a conductive silver paste. The substrate has a circularly shaped sensing area of interdigitated Pt electrodes with a 20 μm spacing that is encircled by a Pt heater to regulate and ensure the uniformity of the operating temperature. The $ZnSnO_3$ solution was drop cast onto the active area of the microsensors and heated at 90 °C for 15 min to evaporate the solvent, followed by calcination at 400 °C using an electric furnace in the air for 2 h to stabilize the sample before the gas-sensing measurements. Photos of the system are shown in Fig. S2 (ESI†). The microsensor electrode was wire-bonded in a ceramic package and placed in a sensor chamber for electrical measurements.

The $ZnSnO_3$ sensor was exposed to various gases, namely CO_2 (2000 ppm in N_2), formaldehyde (20 ppm in N_2), NO_2 (21 ppm in N_2), H_2 (5% in N_2), and CO (500 ppm in N_2), which were calibrated and supplied by Praxair, Inc. A LabView-controlled gas-delivery system was used to control the total flow rate of 300 sccm to the sensor chamber. The sensor signal was analyzed using a data-acquisition system (LabView) with an open-source Java-based instrument (Zephyr) for controlling and obtaining the data.[37–39] The sensor measurements were conducted using a

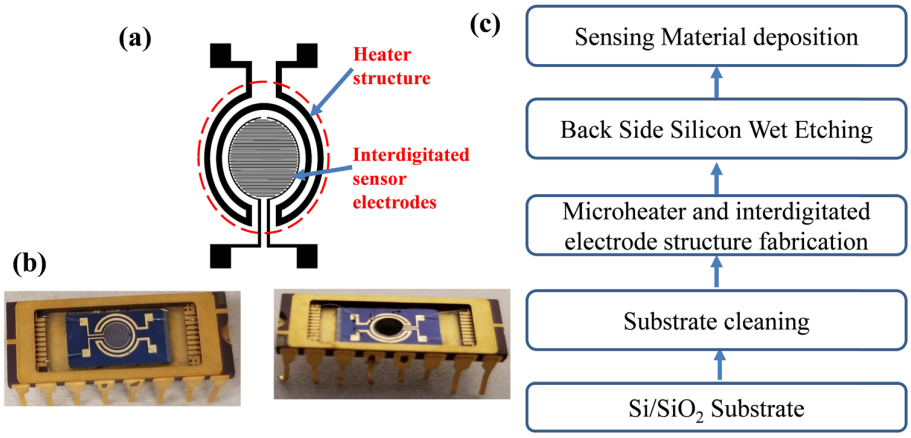

Fig. 1 (a) Schematic illustration of the sensor device. (b) Zinc stannate microcubes with (left) and without (right) the integrated microheater sensor. (c) Microsensor fabrication process.

Keithley 2602 source meter by applying a bias voltage and recording the current, from which the resistance R was calculated. The gas-sensing parameters obtained were the sensor response, which is defined as $S\ (\%) = (R_g - R_a)/R_a \times 100$, where R_g and R_a are the resistance of the sensor film under exposure to the test gas and to fresh air, respectively; the response time (τ_{res}), which is defined as the time to reach 90% of the full response after exposure to the target gas; and the recovery time (τ_{rec}), which is defined as the time to return to 10% of the baseline resistance after the target gas flow is stopped.

3. Results and discussion

3.1 Microstructural and structural characterization

Phase identification was performed using the X-ray powder diffraction (XRD) method, where the diffraction pattern is shown in Fig. 2a. The crystal structure of $ZnSnO_3$ in Fig. 2b was refined using the Fullprof Rietveld analysis program. The XRD data for the refinement were collected at room temperature in the 2θ range from 10 to 100° with a step size of 0.01°. Peak profiles were fitted using the pseudo-Voigt function. $ZnSnO_3$ crystals have a rhombohedral crystal symmetry in the $R3c$ (C_{3v}) (space group no. 161) crystallographic point group, where the Sn atom sits at the origin.[40,41] The structural parameters from the Rietveld analysis are listed in Table 1. The absence of sharp peaks in the diffraction pattern indicated the presence of amorphous $ZnSnO_3$. However, the Bragg positions from the Rietveld refinement were matched with the JCPDS file no. 52-1381, confirming a perovskite structure without impurities. The as-prepared sample was shown to be pure crystalline $ZnSn(OH)_6$ (Fig. S3, ESI†), and this crystalline to amorphous change of the solid microcubes was observed after calcination at 450 °C for 2 h.[29] Basically, $ZnSn(OH)_6$ was dehydrated during

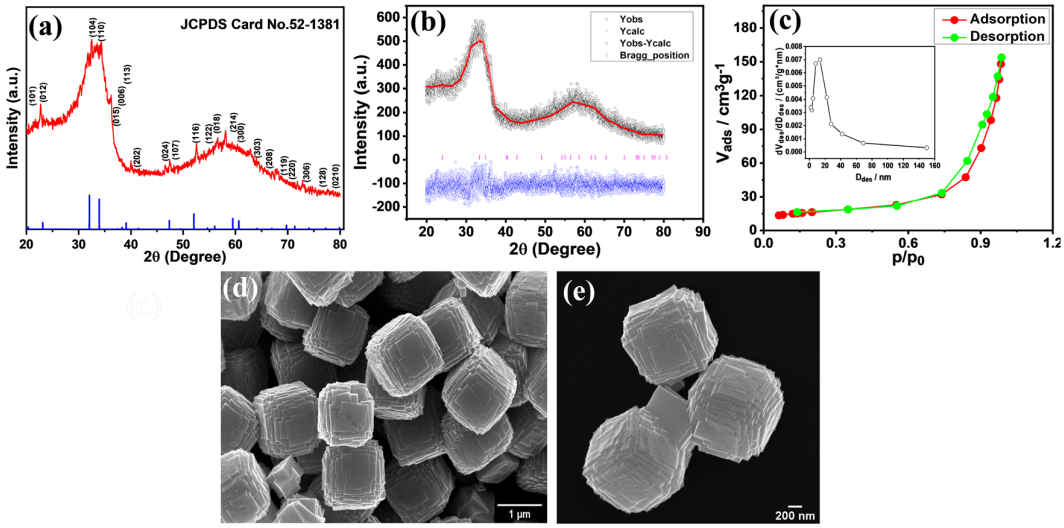

Fig. 2 (a) X-ray diffractogram of as-prepared $ZnSnO_3$ microcubes; (b) Rietveld refinement of the $ZnSnO_3$ sample; (c) nitrogen adsorption–desorption isotherm of the $ZnSnO_3$ microcubes; and (d and e) low- and high-resolution SEM images, respectively, of the $ZnSnO_3$ microcubes.

Table 1 Structural parameters from Rietveld analysis

Composition	Lattice constant (Å)	c^2	Zn coordinates	Sn coordinates	O coordinates	Cell volume (Å^3)
$ZnSnO_3$	$a = b = 5.1378$ $c = 13.4987$	2.01	$x = 0.0000$ $y = 0.0000$ $z = 0.2500$	$x = 0.000$ $y = 0.000$ $z = 0.000$	$x = 0.0410$ $y = 0.3333$ $z = 0.0833$	308.274

the calcination process, and the original hydrogen–oxygen bonds in the structure were destroyed. This resulted in a large number of dangling bonds on the surface and disordering the internal lattice, thus forming amorphous $ZnSnO_3$. Because of the significant number of dangling bonds, the amorphous $ZnSnO_3$ has a larger specific surface area and exhibits superior catalytic activity compared with that of the crystallized form.[42,43] Fig. 2c shows the N_2 adsorption–desorption isotherms for the $ZnSnO_3$ microcubes, from which a specific surface area of 56.3 $m^2\ g^{-1}$ and a pore volume of 0.218 $m^3\ g^{-1}$ were calculated. The pore-size distribution derived from the desorption data and estimated from the isotherm using the Barrett–Joyner–Halenda (BJH) model (inset in Fig. 2c) indicates a pore diameter ranging from 3 to 92 nm, with an average size of 20 nm. The morphological features of the $ZnSnO_3$ sample are illustrated in Fig. 2(d and e), where the high- and low-resolution FESEM images show uniform microcubes with an average size of 1–1.2 μm. Elemental analysis and mapping recorded in the EDS analysis (Fig. S4, ESI†) revealed the elemental distribution of Zn, Sn, and O elements without any impurities. Notably, the homogeneous dispersion of the elements was confirmed in addition to Si from the substrate.

The chemical states and chemical composition of the $ZnSnO_3$ microcubes are depicted in the XPS spectra of Fig. 3. The survey spectrum in Fig. 3a reveals the presence of Zn, Sn, and O elements, without any types of impurities. The high-resolution XPS spectra of Zn 2p, Sn 3d, and O 1s after Gaussian fitting are shown in Fig. 3b–d, respectively. Two main peaks of Zn $2p_{3/2}$ and Zn $2p_{1/2}$ appear at 1021.6 and 1044.7 eV, respectively, in Fig. 3b.[44] The well-resolved Sn 3d spectrum in Fig. 3c features peaks at 494.8 and 486.3 eV, which are assigned to Sn $3d_{3/2}$ and Sn $3d_{5/2}$, respectively, owing to the Sn^{4+} ions.[45] Fig. 3d shows the O 1s spectrum, which is deconvoluted into two peaks (O_I and O_{II}). The binding energy of 530.6 eV for O 1s is attributed to the metal–oxygen bonding, and the other peak at 532.2 eV is due to the oxygen of surface hydroxyl groups (O–H) and chemisorbed oxygen on the semiconductor.[46,47]

3.2 Gas-sensing properties

The gas-sensing performance of the $ZnSnO_3$ microcubes for NO_2 gas is illustrated in Fig. 4. The operating temperature is known to play a major role in metal oxides because it affects the sensor response/recovery speed *via* gas adsorption/desorption processes. Fig. 4a shows the effect of temperature on the sensor response time for 10 ppm NO_2 ($n = 4$). For the $ZnSnO_3$ semiconductor, oxygen is adsorbed onto the metal oxide surfaces in the air to attract electrons from the grains, forming oxygen species (O^-, O^{2-}, O_2^-, *etc.*) between 100 and 300 °C. At low temperatures the reaction rate is low, yielding a low sensor response. With an increased temperature, the thermal energy provided is sufficient to overcome the activation-energy barrier

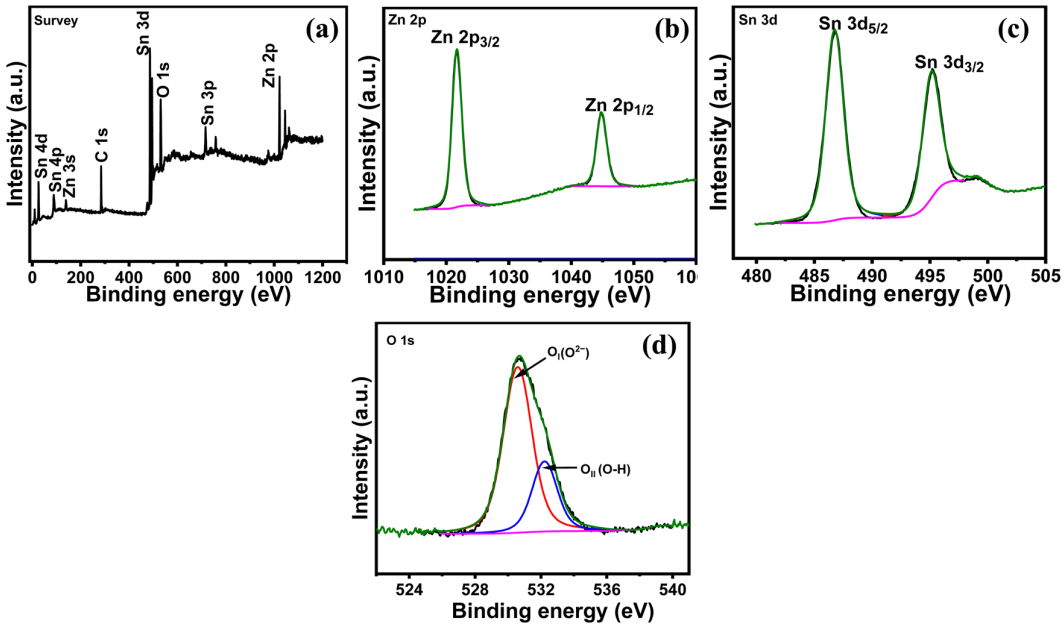

Fig. 3 (a) XPS survey spectrum; (b) Zn 2p spectrum; (c) Sn 3d spectrum; and (d) O 1s spectrum for the $ZnSnO_3$ microcubes.

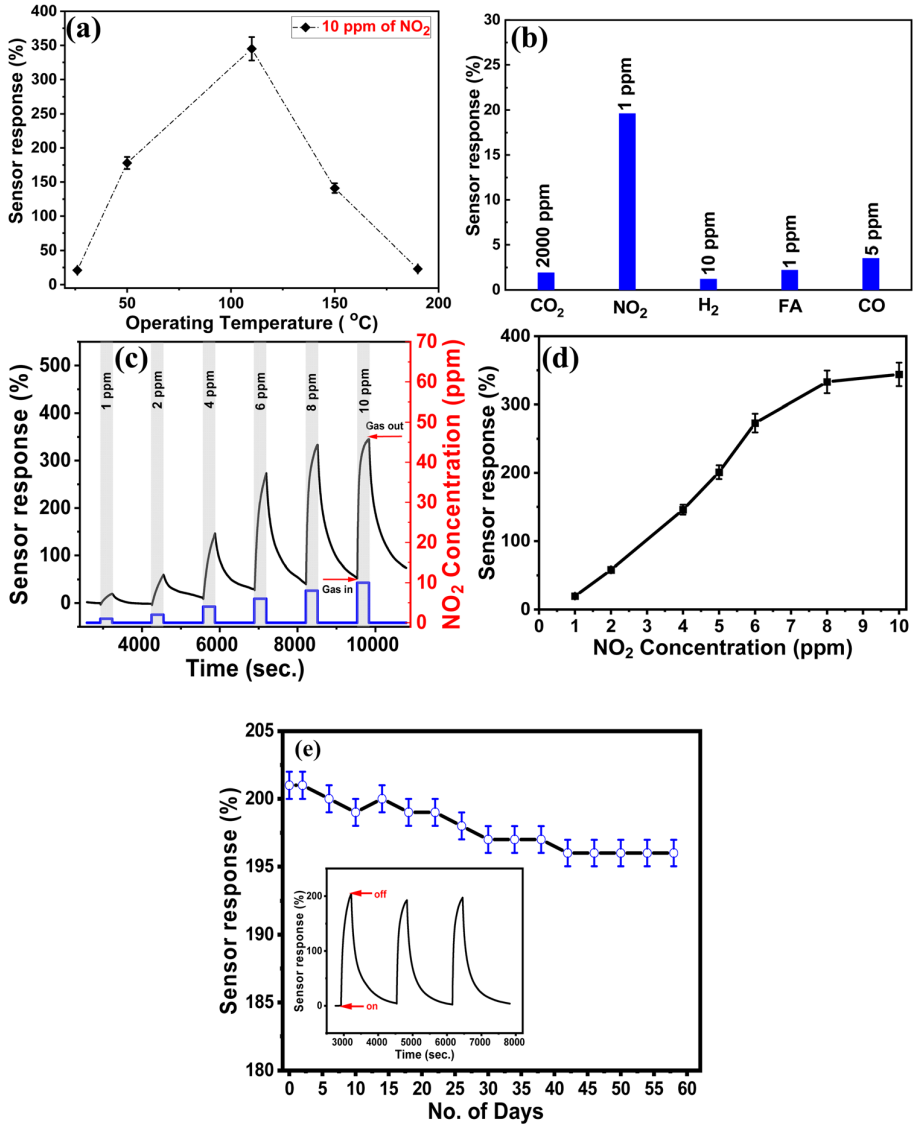

Fig. 4 (a) Temperature-dependent response of the $ZnSnO_3$ sensor exposed to 10 ppm of NO_2 gas (n = 4). (b) Selectivity plot of the $ZnSnO_3$ sensor to different oxidising and reducing gases at 110 °C. (c) Dynamic sensing response of the $ZnSnO_3$-based sensor to 1–10 ppm of NO_2 gas at 110 °C. (d) Gas concentration-dependent sensor response of the $ZnSnO_3$-based sensor to 1–10 ppm NO_2 gas at 110 °C by performing a number of experiments (n = 10). (e) Long-term stability testing of the $ZnSnO_3$-based sensor with exposure to 5 ppm of NO_2 gas. The reproducibility of the sensor for 3 cycles of exposure to 5 ppm NO_2 is illustrated in the inset (n = 8).

for surface reaction, which increases the reaction rate and the sensor response with respect to NO_2. Above 110 °C, the rate of desorption of chemisorbed oxygen is higher than the reaction rate, thus leading to a decline in the response, as also observed in other studies.[13] Hence, the optimum operating temperature (OT) for the detection of NO_2 is 110 °C. The histogram in Fig. 4b for toxic oxidizing/reducing gases indicates significant selectivity for NO_2 owing to the rapid reaction rate of NO_2 molecules on the sensor surface. Fig. 4c shows sensing cycles for NO_2 at 110 °C, with increasing signals for higher concentrations. The $ZnSnO_3$ sensor displays a peak response of 342% upon the exposure to 10 ppm of NO_2 and 19% for exposure to NO_2 at 1 ppm. Fig. 4d shows the sensor response of the $ZnSnO_3$ microcubes with respect to the NO_2 concentration from 1 to 10 ppm at 110 °C (n = 10). In the low-concentration region, the sensor response was relatively linear up to 8 ppm. This could be caused by saturation of the sites for adsorption and the lack of surface-adsorbed oxygen. The sensor response saturates and reaches a maximum at NO_2 concentrations higher than 10 ppm (see Fig. 4(d)). As the threshold limit for NO_2 gas was 10 ppm, we varied the concentration from 1 to 10 ppm, and due to the accuracy of the mass flow controllers in the gas-delivery system, the lowest concentration of NO_2 that could be reliably delivered was 1 ppm. The limit of detection is based on the noise level during data

Table 2 Comparison of NO_2-sensing properties for the $ZnSnO_3$ compound with other materials

Materials	Concentration (ppm)	Sensor response	Operating temp. (°C)	Response/recovery time (s)	Ref.
Zn_2SnO_4	40	29.3[a]	200	8/58	30
$ZnSnO_3$	80	12.05[b]	RT (under UV-LED)	169/217	31
Zn_2SnO_4	200	2.66[c]	200	25/326	48
Pd-Zn_2SnO_4	200	3.31[c]	200	5/179	48
Zn_2SnO_4/ZnO	1	173.26[a]	300	90/130	49
Zn_2SnO_4	1	102.21[a]	300	150/160	49
Zn_2SnO_4	5	118.45[a]	300	100/120	49
Zn_2SnO_4	5	110[b]	400	NR	50
rGO@Zn_2SnO_4	5	240[b]	30	NR	50
Pd–ZnO	1	13.5[a]	100	141/177	51
Ag–Fe_2O_3	4	3.5[a]	150	NR	52
Pt–WO_3	1	11.24[a]	150	27/34	53
$ZnSnO_3$	0.8	1.89[a]	125	NR	54
Pt–$ZnSnO_3$	0.5	16.0[a]	125	9/82	54
$ZnSnO_3$	1	19.7	110	40/140	This work

[a] Response: (R_g/R_a). [b] $\Delta R/R_a = |R_g - R_a|/R_a$. [c] $(R_a - R_g)/R_a$.

collection; more specifically, the noise level is calculated from the resistance of the sensor in air for a duration of 10 min. Based on the sensor response at 1 ppm, using a typical signal-to-noise threshold of 3, the calculated detection limit of the sensor is about 85.98 ppb. We also confirmed the reliability and stability of the sensor by performing sensing experiments for up to two months, without noting any change in the sensor response and film morphology (n = 8).

The long-term stability of the sensor was tested for 60 days using a 5 ppm concentration of NO_2 gas at 110 °C. The results in Fig. 4e show good stability, with the sensor response gradually being lowered from 201% to 196% in 60 days. The reproducibility of the sensor response was confirmed *via* three successive cycles of NO_2 at 5 ppm, with little change seen. Furthermore, it was found that the $ZnSnO_3$ microcubes can detect 5 ppm NO_2 with a response time of 3.36 mins and recovery time of 11.7 mins at 110 °C, as shown in Fig. S5a and b (ESI†). Such a high response at a low temperature is rare in the literature, as indicated in Table 2. The working temperature of the pure $ZnSnO_3$ material was observed to be higher because the material requires more activation energy for the detection of NO_2 gas, even at sub-ppm levels. Heteronanostructures or surface-modified zinc stannate has a higher affinity for oxidizing gases, particularly NO_2, favoring its trace-level detection.

3.3. Gas-sensing mechanism of the $ZnSnO_3$ microcubes

The findings can be explained using a gas-sensing mechanism for the $ZnSnO_3$ microcubes for metal oxide gas sensors.[3,35] The mechanism for the $ZnSnO_3$ microcubes and the surface-depletion model for NO_2 gas is illustrated in Fig. 5. It is a surface-controlled process that is regulated by adsorption–desorption in the presence of gas molecules. $ZnSnO_3$ is an n-type semiconductor oxide in which electrons are the majority charge carriers. When the $ZnSnO_3$ microcubes are exposed to air, as in Fig. 5a, oxygen is adsorbed to form O_2^-, O^-, and O^{2-} ion species by trapping/capturing electrons from the conduction band. This decreases the electrical conductivity. At the optimized operating temperature of 110 °C, adsorbed oxygen is mainly present in the O^{2-} form. Fig. 5b shows a schematic diagram of the interaction of O^{2-} ion species and NO_2 gas on the $ZnSnO_3$ surface. The reaction kinetics may be explained by the following reactions:[55–57]

$$O_{2(gas)} \rightarrow O_{2(ads.)} \quad (1)$$

$$O_{2(ads.)} + e^- \rightarrow {O_2}^-_{(ads.)} \quad (2)$$

$${O_2}^-_{(ads.)} + e^- \rightarrow 2{O}^-_{(ads.)} \quad (3)$$

$${O}^-_{(ads.)} + e^- \rightarrow {O}^{2-}_{(ads.)} \quad (4)$$

Upon exposure to NO_2 gas, the gas molecules are absorbed on the $ZnSnO_3$ microcubes and act as acceptors to attract released electrons, as in the following reactions:[58]

$$NO_{2(g)} + e^- \leftrightarrow {NO_2}^-_{(ads.)} \quad (5)$$

$${NO_2}^-_{(ads.)} + {O}^{2-}_{(ads.)} + e^- \leftrightarrow NO(g) + 2{O}^{2-}_{(ads.)} \quad (6)$$

A depletion region is formed on the surface of each $ZnSnO_3$ microcube as a result of these reactions, thus causing the sensor resistance to increase. When the sensors are no longer exposed to NO_2, the resistance values returned to those in the ambient air owing to a decrease in the width and resistance of the depletion layer. In other words, extracted electrons are returned to the conduction band, lowering the sensor resistance.

3.4 Charge-transport properties of $ZnSnO_3$ microcubes

The I–V characteristics of a $ZnSnO_3$ film at different temperatures (Fig. 6a) show that the current decreases when the temperature is decreased since the number of thermally generated charge carriers decreases. The change in resistance (R) with respect to the temperature in Fig. 6b enables the linear fitting of ln (R) *vs.* ($1/T$) in the range of 300–240 K, which means that the electrical conductivity of the $ZnSnO_3$ film follows the Arrhenius law $R = R_0 \exp\left(\frac{E_a}{kT}\right)$, where R_0 is a constant, E_a is the activation energy, and k is the Boltzmann constant.[59,60] The activation energy was determined as ~1.7 eV using the linear portion of the curve. It is well established that the concentration of the intrinsic charge carries decreases with decreasing temperature for semiconductors. Arrhenius's law is expected in the temperature range where the intrinsic charge carriers dominate.[61] Because of the defects or disordered states in the $ZnSnO_3$ film at low temperatures, the hopping transport dominates over band transport. This explains the deviation from the Arrhenius plot at low temperatures.[62,63] Taken together, these results confirm the semiconducting nature of $ZnSnO_3$ films. Moreover, the reported value of the zinc stannate work function is 5.02–5.03 eV.[64,65] To measure the I–V and gas-sensing characteristics, gold electrodes were used since the gold work function is very close to that of zinc stannate, *i.e.*, 5.1 eV.[66] Therefore, gold can make an ohmic contact with zinc stannate.

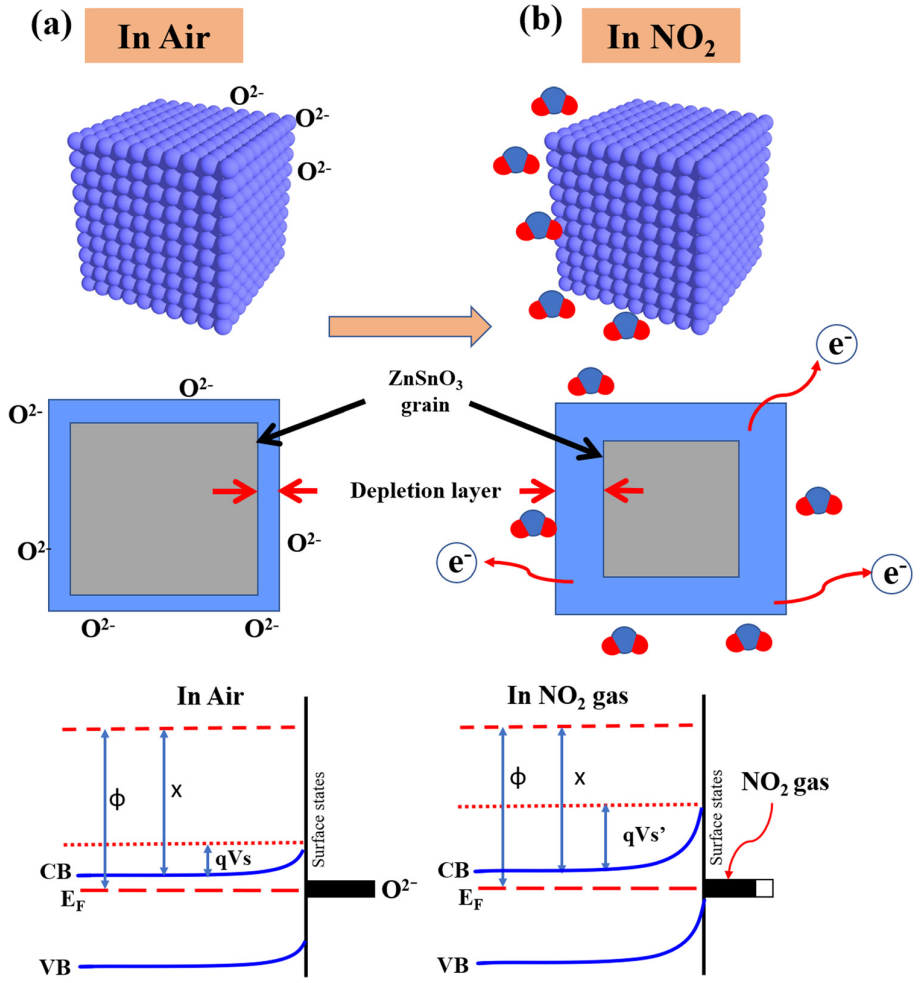

Fig. 5 Schematic illustration of the NO_2-sensing mechanism of the $ZnSnO_3$ sensor.

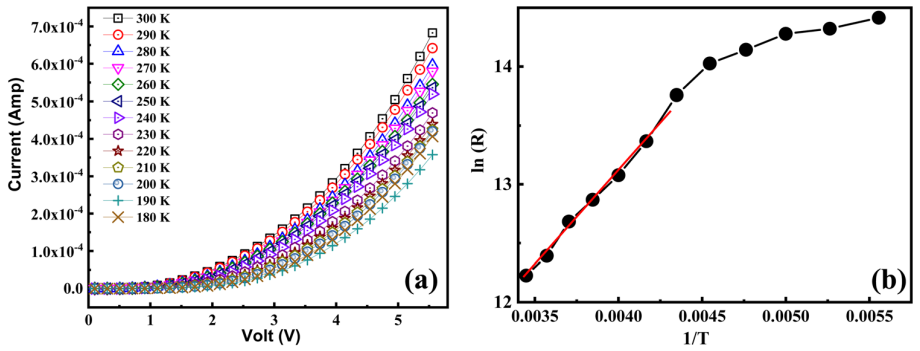

Fig. 6 Temperature-dependent (a) *I*–*V* characteristics, and (b) ln (*R*) *vs.* (1/*T*) plot for a $ZnSnO_3$ film.

4. Conclusion and future studies

We have employed a simple one-step co-precipitation method to fabricate $ZnSnO_3$ microcubes for the detection of NO_2 using a low-power microheater platform. With the advantages of the large surface area of the $ZnSnO_3$ nanostructures, the resulting sensor shows a superior sensing response to NO_2 (an average response of ~344 at 10 ppm) with a fast response and recovery time at a relatively low operating temperature of 110 °C. The sensor exhibited excellent stability for a long period of time as well as high selectivity for NO_2. This facile and versatile

fabrication strategy provides a method for producing low-power gas sensors *via* low-cost mass production. We discovered a few limitations in detecting NO_2 with this material, such as the operation temperature and selectivity, and even it was observed in published articles.[30–32] The sensitivity is very low at room temperature, with a long recovery time and poor selectivity. Many researchers have used strategies such as surface modification, doping, and light illumination to overcome these issues, which we outlined in the introduction. Future approaches to $ZnSnO_3$ sensing characteristics could consider various environmental conditions and more in-depth studies to understand the selectivity fundamentals using XPS and XRD characterization. Moreover, the interactions between the sensing layer and the gas molecules will be analysed using density functional theory (DFT), which will help to overcome the problem of selectivity before actual experiments. Another possibility is to exploit the versatility of $ZnSnO_3$ and design different microsensor units with varied responses to produce an electronic nose (E-nose) on a single chip. This could enable us to overcome the problems of selectivity and operation temperature, as the sensing of NO_2 and other gases would be based on a global selectivity concept.

Conflicts of interest

There are no conflicts to declare.

Acknowledgements

This work was supported by the Director, Office of Science, Office of Basic Energy Sciences, Materials Sciences and Engineering Division, of the US Department of Energy under Contract No. DE-AC02-05-CH11231, within the van der Waals Heterostructures Program (KCWF16), which is provided for gas sensor response characterization. This work was also supported in part by the Berkeley Sensor and Actuator Center (BSAC), an Industry/University Research Cooperation Center. N.J was supported by the Sao Paulo Research Foundation (FAPESP) (grant no. 2014/23546-1, 2016/23474-6, 2018/22214-6, and 2013/07296-2) and CNPq (Brazil).

References

1 J. Samà, G. Domènech-Gil, I. Gràcia, X. Borrisé, C. Cané, S. Barth, F. Steib, A. Waag, J. D. Prades and A. Romano-Rodríguez, Electron beam lithography for contacting single nanowires on non-flat suspended substrates, *Sens. Actuators, B*, 2019, **286**, 616–623, DOI: **10.1016/j.snb.2019.01.040**.

2 *Functional Nanomaterials Advances in Gas Sensing Technologies*, ed. S. Thomas, N. Joshi, V.K. Tomer, Springer, Singapore, 2020, DOI: **10.1007/978-981-15-4810-9**.

3 R. Malik, V. K. Tomer, Y. K. Mishra and L. Lin, Functional gas sensing nanomaterials: A panoramic view, *Appl. Phys. Rev.*, 2020, **7**, 021301, DOI: **10.1063/1.5123479**.

4 R. Malik, V. K. Tomer, N. Joshi, T. Dankwort, L. Lin and L. Kienle, Au–TiO2-Loaded Cubic g-C3N4 Nanohybrids for Photocatalytic and Volatile Organic Amine Sensing Applications, *ACS Appl. Mater. Interfaces*, 2018, **10**, 34087–34097, DOI: **10.1021/acsami.8b08091**.

5 N. Joshi, V. K. Tomer, R. Malik and J. Nie, *Recent Advances on UV-Enhanced Oxide Nanostructures Gas Sensors*, 2020, pp. 143–159, DOI: **10.1007/978-981-15-4810-9_6**.

6 N. Joshi, M. L. Braunger, F. M. Shimizu, A. Riul and O. N. Oliveira Jr., *Two-Dimensional Transition Metal Dichalcogenides for Gas Sensing Applications*, 2020, pp. 131–155, DOI: **10.1007/978-3-030-38101-1_4**.

7 N. Joshi, T. Hayasaka, Y. Liu, H. Liu, O. N. Oliveira Jr. and L. Lin, A review on chemiresistive room temperature gas sensors based on metal oxide nanostructures, graphene and 2D transition metal dichalcogenides, *Microchim. Acta*, 2018, **185**, 213, DOI: **10.1007/s00604-018-2750-5**.

8 X. Chen, T. Wang, J. Shi, W. Lv, Y. Han, M. Zeng, J. Yang, N. Hu, Y. Su, H. Wei, Z. Zhou, Z. Yang and Y. Zhang, A Novel Artificial Neuron-Like Gas Sensor Constructed from CuS Quantum Dots/Bi_2S_3 Nanosheets, *Nano-Micro Lett.*, 2022, **14**(8), DOI: **10.1007/s40820-021-00740-1**.

9 R. Kumar, O. Al-Dossary, G. Kumar and A. Umar, Zinc Oxide Nanostructures for NO2 Gas–Sensor Applications: A Review, *Nano-Micro Lett.*, 2015, **7**, 97–120, DOI: **10.1007/s40820-014-0023-3**.

10 B. Liu, Y. Luo, K. Li, H. Wang, L. Gao and G. Duan, Room-Temperature NO_2 Gas Sensing with Ultra-Sensitivity Activated by Ultraviolet Light Based on SnO_2 Monolayer Array Film, *Adv. Mater. Interfaces*, 2019, **6**(12), 1900376, DOI: **10.1002/admi.201900376**.

11 P. Wang, S. Z. Wang, Q. Han, D. Q. Zou, W. K. Zhao, X. D. Wang, C. Luo, X. Yang, X. Wu and W. F. Xie, Construction of Hierarchical α-Fe2O3/SnO2 Nanoball Arrays with Superior Acetone Sensing Performance, *Adv. Mater. Interfaces*, 2021, **8**(5), 2001831, DOI: **10.1002/admi.202001831**.

12 V. Kruefu, U. Inpan, P. Leangtanom, C. Arkarvipath, P. Kongpark, D. Phokharatkul, A. Wisitsoraat, A. Tuantranont and S. Phanichphant, Enhanced Gas-Sensing Performances of Ru-Loaded p-Type Co3O4 Nanoparticles, Phys. Status Solidi Appl, *Mater. Sci.*, 2018, **215**(20), 1701015, DOI: **10.1002/pssa.201701015**.

13 N. Joshi, L. F. da Silva, F. M. Shimizu, V. R. Mastelaro, J.-C. M'Peko, L. Lin and O. N. Oliveira Jr., UV-assisted chemiresistors made with gold-modified ZnO nanorods to detect ozone gas at room temperature, *Microchim. Acta*, 2019, **186**, 418, DOI: **10.1007/s00604-019-3532-4**.

14 R. Malik, N. Joshi and V. K. Tomer, Advances in the designs and mechanisms of MoO3 nanostructures for gas sensors: a holistic review, *Mater. Adv.*, 2021, **2**, 4190–4227, DOI: **10.1039/D1MA00374G**.

15 N. Joshi, M. L. Braunger, F. M. Shimizu, A. Riul and O. N. Oliveira Jr., Insights into nano-heterostructured materials for gas sensing: A review, *Multifunct. Mater.*, 2021, **4**, 032002, DOI: **10.1088/2399-7532/ac1732**.

16 D. Ma, Y. Su, T. Tian, H. Yin, T. Huo, F. Shao, Z. Yang, N. Hu and Y. Zhang, Highly Sensitive Room-Temperature NO2Gas Sensors Based on Three-Dimensional Multiwalled Carbon

Nanotube Networks on SiO2Nanospheres, *ACS Sustainable Chem. Eng.*, 2020, **8**(37), 13915–13923, DOI: **10.1021/acssuschemeng.0c02707**.

17 B. Zhang, N. Bao, T. Wang, Y. Xu, Y. Dong, Y. Ni, P. Yu, Q. Wei, J. Wang, L. Guo and Y. Xia, High-performance room temperature NO2 gas sensor based on visible light irradiated In2O3 nanowires, *J. Alloys Compd.*, 2021, **867**, 159076, DOI: **10.1016/j.jallcom.2021.159076**.

18 Y. Huang, W. Jiao, Z. Chu, G. Ding, M. Yan, X. Zhong and R. Wang, Ultrasensitive room temperature ppb-level NO2 gas sensors based on SnS_2/rGO nanohybrids with P-N transition and optoelectronic visible light enhancement performance, *J. Mater. Chem. C*, 2019, **7**(28), 8616–8625, DOI: **10.1039/c9tc02436k**.

19 X. Liu, T. Ma, N. Pinna and J. Zhang, Two-Dimensional Nanostructured Materials for Gas Sensing, *Adv. Funct. Mater.*, 2017, **27**(37), 1–30, DOI: **10.1002/adfm.201702168**.

20 J. F. Grajales and A. Baquero-Bernal, Inference of surface concentrations of nitrogen dioxide (NO2) in Colombia from tropospheric columns of the ozone measurement instrument (OMI, *Atmosfera*, 2014, **27**(2), 193–214, DOI: **10.1016/S0187-6236(14)71110-5**.

21 R. Malik, N. Joshi and V. K. Tomer, Functional graphitic carbon(IV) nitride: A versatile sensing material, *Coord. Chem. Rev.*, 2022, **466**, 214611, DOI: **10.1016/j.ccr.2022.214611**.

22 N. Joshi, G. Pransu and C. Adam Conte-Junior, Critical review and recent advances of 2D materials-Based gas sensors for food spoilage detection, *Crit. Rev. Food Sci. Nutr.*, 2022, 1–24, DOI: **10.1080/10408398.2022.2078950**.

23 **https://www.cdc.gov/niosh/pel88/10102-44.html**.

24 J. Xuan, G. Zhao, M. Sun, F. Jia, X. Wang, T. Zhou, G. Yin and B. Liu, Low-temperature operating ZnO-based NO2-sensors: A review, *RSC Adv.*, 2020, **10**(65), 39786–39807, DOI: **10.1039/d0ra07328h**.

25 Q. Li, W. Zeng and Y. Li, Metal oxide gas sensors for detecting NO2 in industrial exhaust gas: Recent developments, *Sens. Actuators, B*, 2022, **359**, 131579, DOI: **10.1016/j.snb.2022.131579**.

26 G. Ibáñez-Redín, N. Joshi, G. F. do Nascimento, D. Wilson, M. E. Melendez, A. L. Carvalho, R. M. Reis, D. Gonçalves and O. N. Oliveira Jr., Determination of p53 biomarker using an electrochemical immunoassay based on layer-by-layer films with NiFe2O4 nanoparticles, *Microchim. Acta*, 2020, **187**, 619, DOI: **10.1007/s00604-020-04594-z**.

27 N. Joshi, L. F. da Silva, H. S. Jadhav, F. M. Shimizu, P. H. Suman, J.-C. M'Peko, M. O. Orlandi, J. G. Seo, V. R. Mastelaro and O. N. Oliveira Jr., Yolk-shelled ZnCo2O4 microspheres: Surface properties and gas sensing application, *Sens. Actuators, B*, 2018, **257**, 906–915, DOI: **10.1016/j.snb.2017.11.041**.

28 N. Joshi, L. F. Da Silva, H. Jadhav, J.-C. M'Peko, B. B. Millan Torres, K. Aguir, V. R. Mastelaro and O. N. Oliveira Jr., One-step approach for preparing ozone gas sensors based on hierarchical $NiCo_2O_4$ structures, *RSC Adv.*, 2016, **6**(95), 92655–92662, DOI: **10.1039/c6ra18384k**.

29 T. Zhou, T. Zhang, R. Zhang, J. Deng, G. Lu and L. Wang, Highly sensitive sensing platform based on ZnSnO 3 hollow cubes for detection of ethanol, *Appl. Surf. Sci.*, 2017, **400**, 262–268, DOI: **10.1016/j.apsusc.2016.12.183**.

30 M. A. Patil, V. V. Ganbavle, K. Y. Rajpure, H. P. Deshmukh and S. H. Mujawar, Fast response and highly selective nitrogen dioxide gas sensor based on Zinc Stannate thin films, *Mater. Sci.: Energy Technol.*, 2020, **3**, 36–42, DOI: **10.1016/j.mset.2019.11.002**.

31 S. Dabbabi, T. Ben Nasr, A. Madouri, A. Cavanna, A. Garcia-Loureiro and N. Kamoun, Fabrication and Characterization of Sensitive Room Temperature NO2 Gas Sensor Based on ZnSnO3 Thin Film, Phys. Status Solidi Appl, *Mater. Sci.*, 2019, **216**(16), 1900205, DOI: **10.1002/pssa.201900205**.

32 P. Wadkar, D. Bauskar and P. Patil, High performance H2 sensor based on ZnSnO3 cubic crystallites synthesized by a hydrothermal method, *Talanta*, 2013, **105**, 327–332, DOI: **10.1016/j.talanta.2012.10.051**.

33 J. Xu, X. Jia, X. Lou and J. Shen, One-step hydrothermal synthesis and gas sensing property of ZnSnO3 microparticles, *Solid State Electron.*, 2006, **50**(3), 504–507, DOI: **10.1016/j.sse.2006.02.001**.

34 X. Jia, M. Tian, R. Dai, D. Lian, S. Han, X. Wu and H. Song, One-pot template-free synthesis and highly ethanol sensing properties of ZnSnO3 hollow microspheres, *Sens. Actuators, B*, 2017, **240**, 376–385, DOI: **10.1016/j.snb.2016.08.146**.

35 Y. Yin, F. Li, N. Zhang, S. Ruan, H. Zhang and Y. Chen, Improved gas sensing properties of silver-functionalized ZnSnO3 hollow nanocubes, *Inorg. Chem. Front.*, 2018, **5**(9), 2123–2131, DOI: **10.1039/c8qi00470f**.

36 A. T. Güntner, V. Koren, K. Chikkadi, M. Righettoni and S. E. Pratsinis, E-Nose Sensing of Low-ppb Formaldehyde in Gas Mixtures at High Relative Humidity for Breath Screening of Lung Cancer, *ACS Sens.*, 2016, **1**(5), 528–535, DOI: **10.1021/acssensors.6b00008**.

37 Y. Wu, N. Joshi, S. Zhao, H. Long, L. Zhou, G. Ma, B. Peng, O. N. Oliveira Jr., A. Zettl and L. Lin, NO2 gas sensors based on CVD tungsten diselenide monolayer, *Appl. Surf. Sci.*, 2020, **529**, 147110, DOI: **10.1016/j.apsusc.2020.147110**.

38 W. S. Chi, C. S. Lee, H. Long, M. H. Oh, A. Zettl, C. Carraro, J. H. Kim and R. Maboudian, Direct Organization of Morphology-Controllable Mesoporous SnO2 Using Amphiphilic Graft Copolymer for Gas-Sensing Applications, *ACS Appl. Mater. Interfaces*, 2017, **9**(42), 37246–37253, DOI: **10.1021/acsami.7b07823**.

39 H. Long, S. Turner, A. Yan, H. Xu, M. Jang, C. Carraro, R. Maboudian and A. Zettl, Plasma assisted formation of 3D highly porous nanostructured metal oxide network on microheater platform for Low power gas sensing, *Sens. Actuators, B*, 2019, **301**, 127067, DOI: **10.1016/j.snb.2019.127067**.

40 H. Wang, H. Huang and B. Wang, First-principles study of structural, electronic, and optical properties of $ZnSnO_3$, *Solid State Commun.*, 2009, **149**(41–42), 1849–1852, DOI: **10.1016/j.ssc.2009.07.009**.

41 Y. Inaguma, M. Yoshida and T. Katsumata, A polar oxide ZnSnO3 with a LiNbO3-type structure, *J. Am. Chem. Soc.*, 2008, **130**(21), 6704–6705, DOI: **10.1021/ja801843v**.

42 X. Wang, M. Li, B. Ding, Y. Liu and T. Chen, UV-enhanced ethanol-sensing properties of TiO2-decorated ZnSnO3 hollow microcubes at low temperature, *J. Mater. Sci.: Mater. Electron.*, 2017, **28**(17), 12399–12407, DOI: **10.1007/s10854-017-7060-x**.

43 Q. Ge, C. Liu, Y. Zhao, N. Wang, X. Zhang, C. Feng, S. Zhang, H. Wang, W. Jiang, S. Liu, W. Ding and C. Dong, Phase evolution in preparing $ZnSnO_3$ powders by precipitation method, *Appl. Phys. A: Mater. Sci. Process.*, 2021, **127**(89), DOI: **10.1007/s00339-020-04244-4**.

44 Q. Xie, Y. Zhao, H. Guo, A. Lu, X. Zhang, L. Wang, M. S. Chen and D. L. Peng, Facile preparation of well-dispersed CeO2-ZnO composite hollow microspheres with enhanced catalytic activity for co oxidation, *ACS Appl. Mater. Interfaces*, 2014, **6**(1), 421–428, DOI: **10.1021/am404487b**.

45 Y. Wang and T. Chen, Nonaqueous and template-free synthesis of Sb doped SnO2 microspheres and their application to lithium-ion battery anode, *Electrochim. Acta*, 2009, **54**(13), 3510–3515, DOI: **10.1016/j.electacta.2008.11.039**.

46 D. Liu, Y. Lv, M. Zhang, Y. Liu, Y. Zhu, R. Zong and Y. Zhu, Defect-related photoluminescence and photocatalytic properties of porous ZnO nanosheets, *J. Mater. Chem. A*, 2014, **2**, 15377–15388, DOI: **10.1039/C4TA02678K**.

47 A. Kumar, N. Joshi, S. Samanta, A. Singh, A. K. Debnath, A. K. Chauhan, M. Roy, R. Prasad, K. Roy, M. M. Chehimi, D. K. Aswal and S. K. Gupta, Room temperature detection of H_2S by flexible gold-cobalt phthalocyanine heterojunction thin films, *Sens. Actuators, B*, 2015, **206**, 653–662, DOI: **10.1016/j.snb.2014.09.074**.

48 V. V. Ganbavle, M. A. Patil, H. P. Deshmukh and K. Y. Rajpure, Development of Zn2SnO4 thin films deposited by spray pyrolysis method and their utility for NO2 gas sensors at moderate operating temperature, *J. Anal. Appl. Pyrolysis*, 2014, **107**, 233–241, DOI: **10.1016/j.jaap.2014.03.006**.

49 S. Park, S. An, H. Ko, C. Jin and C. Lee, Enhanced NO_2 sensing properties of Zn_2SnO_4-core/ZnO-shell nanorod sensors, *Ceram. Int.*, 2013, **39**, 3539–3545, DOI: **10.1016/j.ceramint.2012.10.178**.

50 V. P. Dinesh and P. Biji, Highly sensitive, graphene oxide supported zinc stannate (Zn_2SnO_4) nanocubes and their room temperature NO2 gas sensor properties, in: 2015 IEEE SENSORS - Proc., 2015, DOI: **10.1109/ICSENS.2015.7370359**.

51 X. Chen, Y. Shen, P. Zhou, S. Zhao, X. Zhong, T. Li, C. Han, D. Wei and D. Meng, NO_2 sensing properties of one-pot-synthesized ZnO nanowires with Pd functionalization, *Sens. Actuators, B*, 2019, **280**, 151–161, DOI: **10.1016/j.snb.2018.10.063**.

52 A. Mirzaei, K. Janghorban, B. Hashemi, M. Bonyani, S. G. Leonardi and G. Neri, A novel gas sensor based on Ag/Fe_2O_3 core-shell nanocomposites, *Ceram. Int.*, 2016, **42**(16), 18974–18982, DOI: **10.1016/j.ceramint.2016.09.052**.

53 H. Liu, Y. Xu, X. Zhang, W. Zhao, A. Ming and F. Wei, Enhanced NO_2 sensing properties of Pt/WO3 films grown by glancing angle deposition, *Ceram. Int.*, 2020, **46**(13), 21388–21394, DOI: **10.1016/j.ceramint.2020.05.236**.

54 Y. Yin, Y. Shen, S. Zhao, A. Li, R. Lu, C. Han, B. Cui and D. Wei, Enhanced detection of ppb-level NO_2 by uniform Pt-doped $ZnSnO_3$ nanocubes, *Int. J. Miner., Metall. Mater.*, 2022, **29**, 1295–1303, DOI: **10.1007/s12613-020-2215-9**.

55 L. Yu, F. Guo, S. Liu, B. Yang, Y. Jiang, L. Qi and X. Fan, Both oxygen vacancies defects and porosity facilitated NO2 gas sensing response in 2D ZnO nanowalls at room temperature, *J. Alloys Compd.*, 2016, **682**, 352–356, DOI: **10.1016/j.jallcom.2016.05.053**.

56 C. Fan, J. Shi, Y. Zhang, W. Quan, X. Chen, J. Yang, M. Zeng, Z. Zhou, Y. Su, H. Wei and Z. Yang, Fast and recoverable NO2 detection achieved by assembling ZnO on Ti3C2Tx MXene nanosheets under UV illumination at room temperature, *Nanoscale*, 2022, **14**(9), 3441–3451, DOI: **10.1039/d1nr06838e**.

57 Z. Yang, W. Cao, C. Peng, T. Wang, B. Li, H. Ma, Y. Su, Z. Zhou, J. Yang and M. Zeng, Construction, Application and Verification of a Novel Formaldehyde Gas Sensor System Based on Ni-Doped SnO2Nanoparticles, *IEEE Sens. J.*, 2021, **21**(9), 11023–11030, DOI: **10.1109/JSEN.2021.3053407**.

58 N. Devabharathi, A. M. Umarji and S. Dasgupta, Fully Inkjet-Printed Mesoporous SnO2-Based Ultrasensitive Gas Sensors for Trace Amount NO2Detection, *ACS Appl. Mater. Interfaces*, 2020, **12**(51), 57207–57217, DOI: **10.1021/acsami.0c14704**.

59 X. Li, Z. T. Song, D. L. Cai, X. G. Chen and X. L. Jia, An SPICE model for PCM based on Arrhenius equation, *Chin. Phys. Lett.*, 2009, **26**(12), DOI: **10.1088/0256-307X/26/12/128501**.

60 A. Pirovano, A. L. Lacaita, F. Pellizzer, S. A. Kostylev, A. Benvenuti and R. Bez, Low-field amorphous state resistance and threshold voltage drift in chalcogenide materials, *IEEE Trans. Electron Devices*, 2004, **51**(5), 714–719, DOI: **10.1109/TED.2004.825805**.

61 B. Wei, R. Spolenak, P. Kohler-Redlich, M. Rühle and E. Arzt, Electrical transport in pure and boron-doped carbon nanotubes, *Appl. Phys. Lett.*, 1999, **74**(21), 3149–3151, DOI: **10.1063/1.124093**.

62 C. Michel, S. D. Baranovskii, P. J. Klar, P. Thomas and B. Goldlücke, Strong non-Arrhenius temperature dependence of the resistivity in the regime of traditional band transport, *Appl. Phys. Lett.*, 2006, **89**(11), DOI: **10.1063/1.2348771**.

63 I. P. Zvyagin, On the Theory of Hopping Transport in Disordered Semiconductors, *Phys. Status Solidi*, 1973, **58**(2), 443–449, DOI: **10.1002/pssb.2220580203**.

64 A. Kurz and M. A. Aegerter, Novel transparent conducting sol-gel oxide coatings, *Thin Solid Films*, 2008, **516**(14), 4513–4518, DOI: **10.1016/j.tsf.2007.05.082**.

65 S. Cai, Y. Li, X. Chen, Y. Ma, X. Liu and Y. He, Optical and electrical properties of Ta-doped ZnSnO3 transparent conducting films by sol–gel, *J. Mater. Sci.: Mater. Electron.*, 2016, **27**(6), 6166–6174, DOI: **10.1007/s10854-016-4544-z**.

66 A. K. Mahapatro and S. Ghosh, Schottky energy barrier and charge injection in metal/copper- phthalocyanine/metal structures, *Appl. Phys. Lett.*, 2002, **80**(25), 4840–4842, DOI: **10.1063/1.1483388**.

